JOURNAL OF THERMOPHYSICS AND HEAT TRANSFER
Vol. 22, No. 4, October–December 2008

Simulation of Homogeneous Ethanol Condensation in Nozzle Flows Using a Kinetic Method

Alison C. Gallagher-Rogers,* Jiaqiang Zhong,† and Deborah A. Levin‡
Pennsylvania State University, University Park, Pennsylvania 16802

DOI: 10.2514/1.34451

When a liquid rocket engine operates in the space environment, droplets have been observed in the thruster plume that can cause contamination of spacecraft surfaces. Condensation can add to this contamination by contributing to the formation and growth of liquid particles in the flow. The condensation process has been modeled using the direct simulation Monte Carlo method. Models have been developed and incorporated into the direct simulation Monte Carlo code for the processes involved in condensation, which include nucleation, condensation, evaporation, coalescence, and nonsticking collisions. The models are applied to simulate the flow of ethanol in dry air, which has been used to model hydrazine in contamination studies in a vacuum chamber and has been used in several studies of condensation in a supersonic nozzle. Simulations are conducted of the internal flow in the divergent portion of a supersonic nozzle. The results show reasonable agreement with experimental data for the mass fraction of condensed ethanol along the nozzle axis, but the simulations give a lower value in all cases. The simulation results for the point of condensation onset show good agreement with the experimental data. The results are shown to be sensitive to the nucleation and evaporation rates, as well as the inclusion of the carrier gas.

Nomenclature

C	=	condensation rate, s^{-1}
c	=	velocity, m/s
d	=	cluster diameter, m
E	=	evaporation rate, s^{-1}
E_{int}	=	internal energy, J
E_{kin}	=	kinetic energy, J
F	=	number of real particles per simulated particle
H_v	=	heat of vaporization, J/kg
J	=	nucleation rate, s^{-1}
j	=	cluster size
Kn	=	Knudsen number
k	=	Boltzmann's constant, J/K
L	=	energy released due to latent heat, J, or characteristic length, m
m	=	molecule mass, kg
N	=	number of particles
P	=	pressure, Pa
q	=	sticking probability
R	=	gas constant, J/(kg K)
Re	=	Reynolds number
r	=	cluster radius, m
S	=	degree of supersaturation
T	=	temperature, K
V	=	cell volume, m^3
v	=	velocity, m/s
W	=	weighting factor
We	=	Weber number
X	=	number of cells in the axial direction
x	=	distance in the axial direction, m
Y	=	number of cells in the radial direction
y	=	distance in the radial direction, m
δ	=	velocity boundary-layer thickness, m
ΔF	=	change in free energy, J
Δt	=	time step size, s
Θ	=	characteristic temperature, K
λ	=	mean free path, m
ν	=	constant related to species viscosity
ξ	=	number of internal degrees of freedom
ρ	=	liquid density, kg/m^3
σ	=	surface tension, J/m^2, or collision cross section
ω	=	ethanol mass fraction

Subscripts

0	=	stagnation state
1	=	precollision
2	=	postcollision
c	=	cluster
l	=	liquid
m	=	monomer
r	=	rotation
S	=	saturation state
v	=	vibration or vapor

Superscript

$*$	=	critical state

I. Introduction

WHEN a liquid rocket engine is used for attitude control of a spacecraft, there is a concern of contamination due to unburned droplets of propellant in the thruster plume. These droplets have been observed in both the core of the plume and in the backflow region, so that the thruster can potentially contaminate both its own spacecraft and any other vehicles in the area [1,2]. This can cause damage to spacecraft surfaces, which is particularly concerning for sensitive surfaces such as solar panels.

When the flow inside these thruster nozzles and in the plume becomes supersaturated, homogeneous condensation can occur. The clusters of condensed fluid that form through homogeneous condensation can contribute to the problem of contamination. In actual nozzles, the liquid propellant droplets that cause contamination can come from various sources. For example, during

Presented as Paper 4159 at the 39th AIAA Thermophysics Conference, Miami, FL, 25–28 June 2007; received 5 September 2007; revision received 16 May 2008; accepted for publication 17 May 2008.

*Graduate Student, Department of Aerospace Engineering. Student Member AIAA.

†Postdoctoral Researcher, Department of Aerospace Engineering. Member AIAA.

‡Professor, Department of Aerospace Engineering. Associate Fellow AIAA.

transient operation, the fuel pump can release large propellant droplets that travel through the nozzle. In addition, droplets can break off from the cooling film on the wall of the nozzle and enter the plume [1–4]. Condensation is only one of many factors that contribute to the distribution of droplets in the plume. In laboratory experiments designed to measure homogeneous condensation, these other factors do not exist. Therefore, it is possible to model homogeneous condensation and compare the results directly to the experimental results. The accurate modeling of condensation would then be a step toward the accurate modeling of operational factors such as propellant droplets and the resulting contamination.

In this work, the homogeneous condensation of ethanol in a supersonic nozzle is simulated using the direct simulation Monte Carlo (DSMC) method [5]. The two-phase flow of gas and clusters has multiple length scales with that of the gas–cluster collisional processes being in the transitional to rarefied flow regimes. Therefore, a kinetic-based DSMC method, rather than a continuum-based computational fluid dynamics approach, is employed to study the affect of the condensation process on the nozzle flow. Previous studies of homogeneous condensation have focused on argon and water vapor [6]. In this work, ethanol (C_2H_6O) is used, because its physical properties are similar to those of hydrazine, which is commonly used as a propellant for attitude control thrusters. Ethanol was used to model hydrazine in the experiments of Yarygin et al. [7]. The experiments used model thrusters in a vacuum chamber to test the effectiveness of screens to block contaminants from reaching the backflow area of the plume. In addition, many laboratory experiments have been conducted to determine the onset of condensation in ethanol in supersonic nozzles [8–11].

To model homogeneous condensation in DSMC, classical nucleation theory (CNT) was used to determine the rate of nucleation [12,13]. Models were developed that could be incorporated into the DSMC code to simulate the various processes involved in homogeneous condensation in ethanol. The models were then used to conduct simulations based on the experiments of Wegener et al. [8]. The experiments were conducted using a supersonic nozzle for different supply mass fractions of ethanol in dry air, ω. Results from these experiments are given in the form of the mass fraction of condensed ethanol along the nozzle centerline. To the authors' knowledge, this is the first DSMC model that has been developed for homogeneous condensation in an internal nozzle flow.

In addition, the point of condensation onset was determined in the simulations. Many experiments have been conducted to measure the point of condensation onset in ethanol [8–11]. Several different criteria are used to determine the onset of condensation in experiments, including deviation in static pressure or temperature from the isentrope [8,9,14] and an increase in the intensity of scattered light [10,11]. In this work, the onset point was defined as the point at which the condensed mass fraction reaches 1.0×10^{-4}, as in Wegener et al. [8]. The results for condensation onset were be compared with several sets of experimental results.

A discussion of the DSMC models is given in Sec. II. An overview of the DSMC method is given in Sec. II.A, followed by discussions of the choice of nucleation, condensation, and evaporation rates in Sec. II.B and the development of models for the condensation processes in Sec. II.C. Section III contains the presentation and discussion of the results for all simulated cases. A description of the cases to be simulated and the numerical parameters for each case are given in Sec. III.A. The results for the first three cases, with and without condensation, are given in Sec. III.B, as well as a discussion of the impact of the nucleation and evaporation models on the results. The results for the final two cases are given in Sec. III.C. Conclusions are summarized in Sec. IV.

II. Direct Simulation Monte Carlo Models

A. Direct Simulation Monte Carlo Background

The DSMC method is a simulation method that uses a kinetic approach to model a real gas. In a DSMC simulation, a large number of particles, N, are simulated, and each simulated particle is assumed to represent a number of real particles, F. In this work, the DSMC software program SMILE (statistical modeling in a low-density environment) [15] is used. The program uses the majorant frequency scheme to model the particle translation and collision processes. In the kinetic theory of gases, the master kinetic equations are used to characterize the behavior of an N-particle system with binary collisions. Under the conditions for which $N \to \infty$ and molecular chaos is satisfied, the master kinetic equations transform to the Boltzmann equation. The DSMC method, which makes use of these equations, is essentially a numerical method for solving the Boltzmann equation [15].

In DSMC, the state of each particle is defined by its location and velocity vectors. In a given time step, each particle is moved to a new location based on its velocity and the length of the time step. A particle can also collide with another particle in a binary collision. The number of collision pairs is calculated based on the collision relative velocity and collision cross section. The collision pair is accepted based on Bird's acceptance–rejection principle [5]. In this work, collisions are determined by the variable hard sphere (VHS) model [5], in which the collision cross section, σ, is given as

$$\sigma = \sigma_{\text{ref}}(c_{\text{ref}}/c_r)^{2\nu} \tag{1}$$

where c_r is the collision relative velocity, σ_{ref} and c_{ref} are the reference values of collision cross section and velocity, respectively, and ν is a constant related to the species viscosity. The velocities of particles involved in a collision are changed in the same time step based on energy and momentum conservation. The Larsen–Borgnakke model [5] is used to redistribute the translational and internal energies of the collision pair.

B. Nucleation, Condensation, and Evaporation Rates

To incorporate homogeneous condensation into DSMC, models are needed for the formation and growth of condensed particles, or clusters. The formation of clusters, called nucleation, occurs when a vapor exists in a supersaturated state, in which the vapor pressure is higher than the saturation pressure. The supersaturated state is a metastable state that can exist in regions where there are no foreign particles, surfaces, or nuclei. Once a nucleus forms in the region, the condensation process will be set in motion.

Several theories have been developed to model this process. In this work, CNT, one of the oldest and most popular theories, is employed [12,13]. CNT is commonly used because it may be readily evaluated and, in some cases, has shown good agreement with experimental data.

In a supersaturated vapor environment with no nuclei, density fluctuations in the vapor can lead to the formation of a nucleus. The formation of the nucleus is associated with an increase in the free energy of the system. In CNT, the increase in free energy, ΔF, is described by the bulk properties of the condensible species according to Eq. (2):

$$\Delta F = 4\pi r^2\sigma - \tfrac{4}{3}\pi r^3 \rho RT \ln S \tag{2}$$

In Eq. (2), r is the radius of the newly formed cluster, ρ is the density, R is the species–specific gas constant, T is the temperature, and S is the degree of supersaturation. S is defined as

$$S = P/P_s \tag{3}$$

where P is the condensible gas pressure and P_s is the saturation pressure.

The maximum value of ΔF for a particular value of S is associated with a cluster radius known as the critical radius, r^*. The value of r^* can be calculated as

$$r_* = \frac{2\sigma}{\rho RT \ln S} \tag{4}$$

In CNT, nuclei with radii larger than the critical radius are stable and will grow in size by consuming vapor molecules. Nuclei with radii smaller than the critical radius will decay to monomers. Therefore, in the simulations presented in this work, clusters are introduced into

the flow through nucleation at the critical radius. The rate at which the initial nuclei are introduced into the flow, according to CNT, is given as

$$J = \sqrt{\frac{2\sigma}{\pi m^3}}\frac{\rho_v^2}{\rho_l}\exp\left(\frac{-4\pi r_*^2\sigma}{3kT}\right) \tag{5}$$

Equation (5) assumes that the nucleation process does not significantly impact the vapor number density. In this work, however, it will be shown that the vapor number density is significantly impacted in the nucleation region. Therefore, some error may be associated with the use of CNT to model the nucleation process.

Models for condensation and evaporation must also be considered. Condensation is the growth of clusters that occurs when a cluster collides with a condensible gas particle and the gas particle merges with the cluster. In any such collision, there is a probability that the gas particle will merge with the cluster, referred to as the sticking probability, q. The model for this type of collision will be discussed in Sec. II.C.3. The rate of condensation can be approximated by Eq. (6), in which it has been assumed that the vapor molecules are in an equilibrium Maxwellian velocity distribution at the vapor temperature:

$$C = \frac{4\pi r^2 qP}{\sqrt{2\pi mkT_v}} \tag{6}$$

The evaporation rate, Eq. (7), can then be determined by assuming that the cluster of critical size is in a metastable state in which its condensation and evaporation rates are equal:

$$E = \frac{4\pi r^2 P_s}{\sqrt{2\pi mkT_c}}\exp\left(\frac{2\sigma}{\rho RT_c r}\right) \tag{7}$$

Using the nucleation and evaporation rates established in this section, models can be developed for each process that is involved in condensation. These models are described in Sec. II.C.

C. Condensation Models

When modeling homogeneous condensation in DSMC, one must consider several different types of collisions and processes. Collisions can occur between two gas monomers, a cluster and a monomer, or two clusters. In collisions involving a cluster, sticking can occur. In the case of sticking in a cluster–monomer or cluster–cluster collision, the respective processes of condensation and coalescence must also be considered. In addition, the noncollision processes of nucleation and evaporation must be modeled.

Whenever one of these events occurs, mass, momentum, and energy conservation equations are used to determine the new velocities and temperatures of the gas and cluster particles involved. The monomer–monomer collisions are modeled in the standard DSMC code. Models for the cluster–monomer collision, cluster–cluster collision, nucleation, and evaporation processes have been developed by Zhong [6] for the purpose of simulating homogeneous condensation in argon and water flows. In this work, the models have been modified so that they are suitable for use with ethanol. Detailed descriptions of the models for each of the processes are given in this section.

In each process, conservation of energy must be considered. The kinetic and internal energies of a monomer and a cluster are given as

$$E_{\text{kin}_{\text{monomer}}} = \tfrac{1}{2}mv^2 \tag{8}$$

$$E_{\text{int}_{\text{monomer}}} = \tfrac{\xi}{2}kT \tag{9}$$

$$E_{\text{kin}_{\text{cluster}}} = \tfrac{1}{2}mjv^2 \tag{10}$$

$$E_{\text{int}_{\text{cluster}}} = \tfrac{3}{2}jkT \tag{11}$$

where m is the mass of one molecule of the given species, j is the cluster size, v is the velocity, k is Boltzmann's constant, T is the temperature, and ξ is the number of internal degrees of freedom. These definitions will be used to calculate the energy conservation for each process.

In Eq. (9), ξ is equal to the number of vibrational degrees of freedom, ξ_v, plus the number of rotational degrees of freedom, ξ_r. For a diatomic molecule, such as N_2 or O_2, $\xi_r = 2$. For a polyatomic molecule, such as ethanol, $\xi_r = 3$ and ξ_v varies with T according to

$$\xi_v = \frac{2\Theta_v/T}{\exp(\Theta_v/T) - 1} \tag{12}$$

where Θ_v is the characteristic vibrational temperature. The temperature of ethanol in a cluster is significantly lower than Θ_v, and $\xi_v \ll \xi_r$. Therefore, it can be assumed that ethanol molecular vibrational energy is not activated in the condensed flow, and $\xi_v = 0$. A cluster is assumed to have 3 degrees of freedom for rotation.

1. *Monomer–Monomer Collisions*

Collisions between gas monomers are modeled by the standard DSMC code using the variable hard sphere (VHS) model [5]. Monomer–monomer collisions are treated in the same way whether the two colliding monomers are of the same or different species. Momentum and energy transfer can occur, causing changes in the kinetic and internal energies of both molecules. The Larsen–Borgnakke model [5] is used to redistribute the energy to the translational and internal degrees of freedom and to determine the postcollision states of the two monomers.

2. *Cluster–Monomer Nonsticking Collisions*

When a collision occurs between a cluster and a monomer, it can result in either a sticking or nonsticking process. If a noncondensible gas such as air, as is used in this work, is present, then any collision between a monomer of noncondensible gas and a cluster is considered nonsticking. When a collision occurs between a condensible gas (ethanol) monomer and a cluster, the collision can be either sticking or nonsticking, based on a probability known as the sticking coefficient. The modeling of a sticking collision will be discussed in Sec. II.C.3.

In a nonsticking collision, momentum and energy can be transferred but mass cannot; the cluster size does not change. Equations (13) and (14) give the momentum and energy conservation for a nonsticking collision, using the equations for cluster and monomer energy given in Eqs. (8–11):

$$m_m\mathbf{v}_{m1} + m_c j\mathbf{v}_{c1} = m_m\mathbf{v}_{m2} + m_c j\mathbf{v}_{c2} \tag{13}$$

$$\frac{1}{2}m_m v_{m1}^2 + \frac{\xi_{m1}}{2}kT_{m1} + \frac{j}{2}m_c v_{c1}^2 + \frac{3j}{2}kT_{c1} = \frac{1}{2}m_m v_{m2}^2 + \frac{\xi_{m2}}{2}kT_{m2} + \frac{j}{2}m_c v_{c2}^2 + \frac{3j}{2}kT_{c2} \tag{14}$$

In Eqs. (13) and (14) and subsequent equations, the subscript m represents a monomer, c represents a cluster, 1 represents a value before the collision, and 2 represents a value after the collision.

To solve for the postcollisional states of the cluster and monomer, it is assumed that the temperature of the monomer after the collision is equal to the temperature of the cluster after the collision. Because the gas vibrational temperature is low, the number of degrees of freedom of the monomer is the same before and after the collision. Using simple collision theory, the mean kinetic energy in the center of mass system [5] is $2kT_{c1}$. This allows us to calculate the relative velocity after the collision. Using the known values of the cluster and monomer precollisional velocities and temperatures, as well as the cluster size, and the discussion already given, the velocities and temperatures of the collision pair after the collision can be calculated.

3. Condensation

A sticking collision between a cluster and a monomer is referred to as condensation. When a condensation event occurs, the monomer effectively becomes a part of the cluster. The cluster size, j, increases by 1, and a gas particle is removed from the computational domain. In this model, the monomer transfers all of its momentum and energy to the cluster. The momentum and energy conservation for a condensation event are given as

$$m_m \mathbf{v}_{m1} + m_c j \mathbf{v}_{c1} = (m_m + m_c j)\mathbf{v}_{c2} \tag{15}$$

$$\frac{1}{2} m_m v_{m1}^2 + \frac{\xi_{m1}}{2} kT_{m1} + \frac{1}{2} m_c j v_{c1}^2 + \frac{3}{2} jkT_{c1} = \frac{1}{2} m_c (j+1) v_{c2}^2 + \frac{3}{2}(j+1)kT_{c2} \tag{16}$$

The velocities and temperatures of the cluster and monomer before the collision are known. The initial cluster size, j, is known, and the cluster size after the collision is simply $j+1$. Therefore, the postcollisional cluster velocity and temperature can be calculated using Eqs. (15) and (16).

4. Cluster–Cluster Collisions

A cluster–cluster collision is similar to a cluster–monomer collision in that the outcome can be either sticking or nonsticking. A sticking collision between two clusters is referred to as coalescence, whereas a nonsticking collision can result in either a reflexive or stretching separation.

The outcome of a cluster–cluster collision is determined using the Ashgriz–Poo model [16], which has been used to model coalescence in water droplet flows and validated using molecular dynamics simulations [17]. In the Ashgriz–Poo model, three factors affect the outcome of the collision: cluster size ratio, impact parameter, and Weber number. The cluster size ratio is the ratio of the diameter of the smaller cluster to that of the larger cluster. The impact parameter is the normalized distance between the centers of the undisturbed clusters at the point of closest approach, perpendicular to the relative velocity vector. The Weber number, We, is given by

$$We = \rho d v^2 / \sigma \tag{17}$$

where ρ is the liquid density of the cluster, d is the diameter of the smaller cluster, v is the relative velocity of the two clusters, and σ is the liquid surface tension. Coalescence is more likely to occur for smaller values of We [17]. For a detailed description of the modeling of the outcome of a cluster–cluster collision, see [16,17].

If the collision is determined to be nonsticking, the collision is modeled with the standard DSMC collision model, taking into account the masses of each cluster in the collision. If coalescence occurs, the event is treated similarly to condensation. The two clusters combine to form one large cluster. The momentum and energy conservation equations for coalescence are given as

$$m_{c_A} j_{c_A} \mathbf{v}_{c_A 1} + m_{c_B} j_{c_B} \mathbf{v}_{c_B 1} = (m_{c_A} j_{c_A} + m_{c_B} j_{c_B})\mathbf{v}_{c2} \tag{18}$$

$$\frac{1}{2} m_{c_A} v_{c_A 1}^2 + \frac{3}{2} j_{c_A} kT_{c_A 1} + \frac{1}{2} m_{c_B} j_B v_{c_B 1}^2 + \frac{3}{2} j_B kT_{c_B 1} = \frac{1}{2} m_c (j_{c_A} + j_{c_B}) v_{c2}^2 + \frac{3}{2}(j_{c_A} + j_{c_B})kT_{c2} \tag{19}$$

where the subscripts c_A and c_B are used to differentiate between the two clusters.

The velocities, temperatures, and sizes before the collision are known. The cluster size after the collision is given by the sum of the sizes of the two original clusters. The postcollisional velocity and temperature of the new cluster can be calculated using Eqs. (18) and (19), respectively.

5. Nucleation

In the nucleation process, a number of clusters of the critical size are introduced into the computational domain. The nucleation rate and the critical size are determined as described in Sec. II.B. The number of simulated cluster particles to be formed, N_c, is then calculated based on the nucleation rate. The formula for N_c is given by

$$N_c = (J \Delta t V)/(F W_c) \tag{20}$$

where J is the nucleation rate, Δt is the time step, V is the collision cell volume, F is the number of real particles represented by one simulated particle, and W_c is the cluster weighting factor.

Each new cluster is placed at a random location in the cell. From CNT, the cluster is assumed to be in thermal equilibrium with the surrounding gas. Therefore, the cluster temperature and velocity are determined from the local gas conditions. The conditions of the gas in the cell are adjusted to account for the new cluster. If a cluster of size j is formed, j monomers are removed from the cell to conserve mass. To satisfy conservation of energy, the latent heat released by the cluster formation is distributed evenly to each monomer in the cell. The energy released, L, is assumed to have the following form:

$$L = \Delta H_v m j \tag{21}$$

where ΔH_v is the latent heat of vaporization for ethanol.

6. Evaporation

In the evaporation process, monomers are removed from clusters and are placed in the computational domain as separate entities. It is assumed that molecules evaporate from clusters one at a time, so that each evaporation event involves the removal of one monomer from a cluster. When an evaporation event occurs, the cluster size is reduced by one, and one new monomer is randomly placed in the cell. The momentum and energy conservation equations are given as

$$m_c j \mathbf{v}_{c1} = m_m \mathbf{v}_{m2} + m_c (j-1)\mathbf{v}_{c2} \tag{22}$$

$$\frac{1}{2} m_c j v_{c1}^2 + \frac{3}{2} jkT_{c1} = \frac{1}{2} m_c (j-1) v_{c2}^2 + \frac{3}{2}(j-1)kT_{c2} + \frac{1}{2} m_m v_{m2}^2 + \frac{\xi_{m2}}{2} kT_{m2} \tag{23}$$

The velocity, temperature, and size of the cluster before the evaporation are known. The size of the cluster after the evaporation is one less than the initial size. To solve for the velocities and temperatures of the monomer and cluster after the evaporation, two assumptions must be made. First, it is assumed that the temperature of the monomer after the evaporation is equal to the temperature of the cluster before the evaporation. Second, as in Sec. II.C.2, it is assumed that the mean postcollision kinetic energy in the center of mass system is $2kT_{c1}$ [5]. This allows us to calculate the magnitude of the relative velocity after the collision, and the direction of the relative velocity vector is chosen randomly. Then, using Eqs. (22) and (23), the postcollision states of the cluster and monomer can be determined.

III. Simulations

Simulations were conducted to model the homogeneous condensation of ethanol in a supersonic nozzle flow. The simulations are modeled after the experiments of Wegener et al. [8]. The experiments measured the condensation of ethanol in a supersonic nozzle. Air was used as a carrier gas, and experiments were conducted for several different values of the ethanol mass fraction. Experimental data of cluster mass fraction and condensation onset are given.

In this work, the simulation stagnation conditions and nozzle shape are based on these experiments. However, it is not possible to produce a valid DSMC solution at the total pressure used in the

Table 1 Stagnation conditions for experimental and simulation conditions

Experiment and simulation			Experiment [8]			Simulation		
Case	$P_{0_{\text{Ethanol}}}$, Pa	T_0, K	ω	P_0, kPa	$P_{0_{\text{Air}}}$, kPa	ω	P_0, Pa	$P_{0_{\text{Air}}}$, Pa
1	258.73	296	0.005	83.46	83.20	1.000	258.73	0.00
2	258.73	296	0.005	83.46	83.20	0.384	984.75	726.02
3	258.73	296	0.005	83.46	83.20	0.237	1710.77	1452.04
4	416.65	295	0.008	83.33	82.91	0.333	1868.69	1452.04
5	174.99	297	0.0034	83.33	83.16	0.174	1627.03	1452.04

Table 2 Ethanol physical properties (the values and semi-empirical fits are taken from [8])

Molecular weight, g/mol	46.07
Ratio of specific heats	1.13
Saturation pressure, Pa	$6.343 \times 10^{-9} \exp(0.974T(K))$, $T(K) < 170$
	$133.32\ (10^{16.87-5819/T(K)+414{,}300/T(K)^2})$, $170 < T(K) < 219.1$
	$133.32\ (10^{9.760-2371/T(K)})$, $T(K) > 219.1$
Surface tension, J/m^2	$1.0 \times 10^{-3}\ (23.97 - 0.085(T(K) - 273.15))$

experiments, which was approximately 83 kPa. Therefore, simulations were first conducted using pure ethanol at the partial pressures used in the experiments. Small amounts of air were then added to assess the impact of the carrier gas on the ethanol condensation, which will be discussed further.

In this section, the computational setup and numerical parameters are presented. Results are then presented for flow with and without condensation for different amounts of ethanol and carrier gas.

A. Numerical Parameters

Table 1 lists the stagnation conditions for each simulation, as well as the conditions for the corresponding experiment. In Table 1, ω is the ethanol mass fraction, P_0 is the stagnation pressure, T_0 is the stagnation temperature, and $P_{0_{\text{Ethanol}}}$ and $P_{0_{\text{Air}}}$ are the partial pressures at the stagnation condition of ethanol and air, respectively. As discussed, the air pressure in the simulations is much lower than that of the experiments. Note that cases 1–3 correspond to the same experimental case but, in the simulations, cases 1–3 differ by the amount of air. In case 1, no air is used. Case 2 has a small amount of air, and case 3 has twice as much air as case 2. The goal of simulating cases 1–3 is to assess the impact of the carrier gas on the results. Cases 4 and 5 correspond to two more experiments in which the mass fraction of ethanol has been varied. These cases allow us to evaluate how the agreement between the simulation results and the experiments is affected by a change in the amount of ethanol.

The thermodynamic properties of ethanol that are needed for the simulations are listed in Table 2. The equations given for saturation pressure and surface tension are curve fits made by Wegener et al. [8] based on empirical data. The table is adapted from Wegener et al. [8].

The simulated nozzle geometry is similar to that of the experimental nozzle [18], a three-dimensional rectangular shape. The simulated nozzle is axisymmetric and conical with the same circumference as the experimental rectangular nozzle, and only the divergent section of the nozzle is considered in the simulation to facilitate the computations. The computational domain begins at the nozzle throat and extends to approximately 1.25 times the length of the divergent section. Table 3 lists the dimensions that define the nozzle and the computational domain. The gas is introduced into the computational domain from a vertical starting surface located at the throat of the nozzle. The conditions on the starting surface are determined by assuming that the flow is isentropic from the stagnation conditions in the chamber to the sonic state at the throat. The simulated flow expands into a vacuum, which is consistent with the experimental low background pressure. The Knudsen number, Kn, is defined as

$$Kn = \lambda / L \tag{24}$$

where λ is the mean free path and L is the characteristic length, chosen as the nozzle throat diameter in this work. Using the throat diameter as the characteristic length, the Knudsen number ranges from 3.8×10^{-4} (case 4) to 1.0×10^{-3} (case 1) at the nozzle throat and from 1.6×10^{-3} (case 4) to 5.6×10^{-3} (case 1) at the nozzle exit. The small Kn numbers illustrate that it is quite challenging to apply the DSMC method to model the internal nozzle flows, which are in the near continuum region.

In each case, the number of real particles represented by each simulated particle, F, is equal to 10^{10}, and the total number of simulated particles is on the order of 10^6. The weighting factor for the clusters, W_c, is 2.5×10^{-4}. The number of collision cells in the computational domain is 400 in the axial direction and 80 in the radial direction. The cells are allowed to subdivide during the simulation, which results in a total number of cells on the order of 10^5. The length of one time step, Δt, is 5.0×10^{-8} s. The number of time steps before the macroparameters are sampled is 48,000, and the total number of time steps is 100,000.

Numerical tests were conducted to determine that the results were independent of cell size, Δt, and the number of simulated particles. As an example, Fig. 1 shows the cluster mass fraction along the nozzle centerline for case 2 when the number of simulated particles is varied from 1.8×10^6 to 3.6×10^6 and all other parameters are held constant. For the results shown in Fig. 1, the average difference between the two results is less than 6%. Therefore, a value of 1.8×10^6 simulated particles was determined to be sufficient.

Table 3 Nozzle geometry

Throat radius[a], m	6.373×10^{-3}
Exit radius[a], m	1.136×10^{-2}
Length of divergent section[a], m	5.7×10^{-2}
Computational domain length, m	7.0×10^{-2}
Computational domain radius, m	1.4×10^{-2}

[a]Adapted from [18]

B. Results: Cases 1–3

DSMC cases 1–3 are based on the same experimental case and are the focus of this work. Cases 1–3 differ in the amount of air that is present in the simulation. Using these cases, one can compare the DSMC simulation results with the experimental results, as well as assess the impact of the presence of an inert gas on the condensation.

In this section, the results for the three cases without condensation will be discussed first. This allows one to compare the gas flowfields and understand the sensitivity to the addition of the inert gas. The results for case 1 with condensation will then be presented, and the sensitivity of the condensate flowfield to the choices of nucleation and evaporation rates will be discussed. Finally, the results for

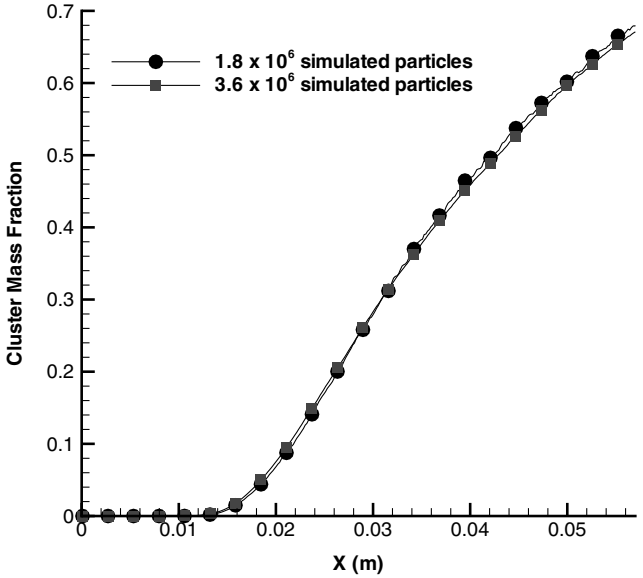

Fig. 1 Cluster mass fraction along the nozzle centerline for case 2 for different numbers of simulated particles.

cases 2 and 3 with condensation will be presented, and the impact of the inert gas on the condensation processes will be explored.

1. *Noncondensation Results*

Cases 1–3 were simulated without condensation using the SMILE DSMC code [15]. In all three cases, the starting surface parameters for the ethanol gas, including number density, temperature, and velocity, are identical. Therefore, the partial pressure of the ethanol gas is the same in all three cases. In case 1, the flow contains pure ethanol. In case 2, air is added to the simulation with a mass fraction of 0.62. In case 3, the amount of air is doubled, bringing the air mass fraction to 0.76. Because the partial pressure of the ethanol remains constant, the gas pressure increases as air is added. By comparing the results from these simulations, one can see how the addition of air impacts the flowfields and anticipate the effect it will have on the condensation.

Figure 2 shows the number density of ethanol gas in the computational domain without condensation, where the nozzle throat is located at $x = 0.0$ m and the nozzle exit is located at $x = 0.057$ m. Comparing the results for cases 1 and 2, one can see that the ethanol gas number density at a given axial location is lower in case 2 than in case 1. This indicates that the expansion is proceeding more quickly due to the higher pressure created by the addition of air. The same trend is observed when comparing cases 2 and 3. However, the difference between cases 2 and 3 is much smaller than the difference between cases 1 and 2. These results suggest that the addition of a small amount of air impacts the flowfield and that adding additional air also impacts the flowfield, but to a lesser degree.

Figures 3–5 show the partial pressure, temperature, and x velocity of the ethanol gas, respectively. These figures illustrate the same trends observed in Fig. 2. When air is added to the flow, the pressure and temperature drop more rapidly and the velocity increases. Figure 5 also shows the impact on the boundary layer inside the nozzle. As the amount of air increases, the boundary-layer thickness decreases. This is consistent with the conclusion that the expansion proceeds more quickly in the higher-pressure cases 2 and 3. This can also be seen in Fig. 6, which shows the x-velocity profile inside the nozzle and the velocity boundary-layer thickness, δ, at two axial locations for cases 1–3. The boundary layer is clearly larger in case 1, when no air is present, and increases as the flow moves toward the nozzle exit, as expected.

The noncondensation results can be used to predict the potential for condensation in the flow. The degree of supersaturation, S, is an indicator of where condensation will occur and is defined by Eq. (3). S is dependent on the species saturation pressure, which varies with

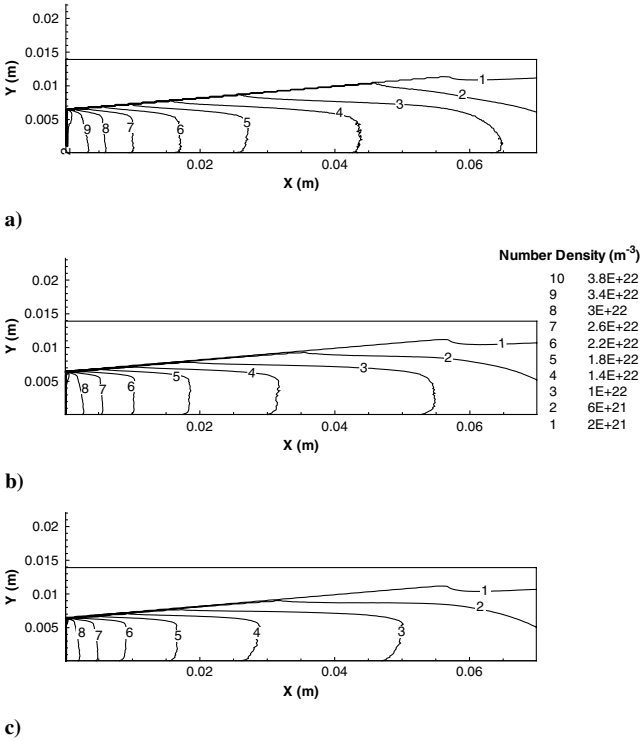

Fig. 2 Ethanol gas number density without condensation: a) case 1, b) case 2, and c) case 3.

temperature. Condensation can occur when P is greater than P_s or S is greater than 1.0. Figure 7 shows the degree of supersaturation near the nozzle throat for cases 1–3 using the saturation pressure curve for ethanol given in Table 2. In case 1, a value of $S = 1.0$ is reached at an axial distance from the throat of about 0.0065 m. In cases 2 and 3, $S = 1.0$ occurs much closer to the throat, at about $x = 0.0022$ and 0.0018 m, respectively. This result is consistent with the previous conclusions because, in cases 2 and 3, the faster drop in temperature and pressure creates conditions that are conducive to condensation closer to the throat. Figure 7 also shows that cases 2 and 3 are more similar to each other than to case 1. Based on these results, condensation can be expected to occur in all cases. It is also expected

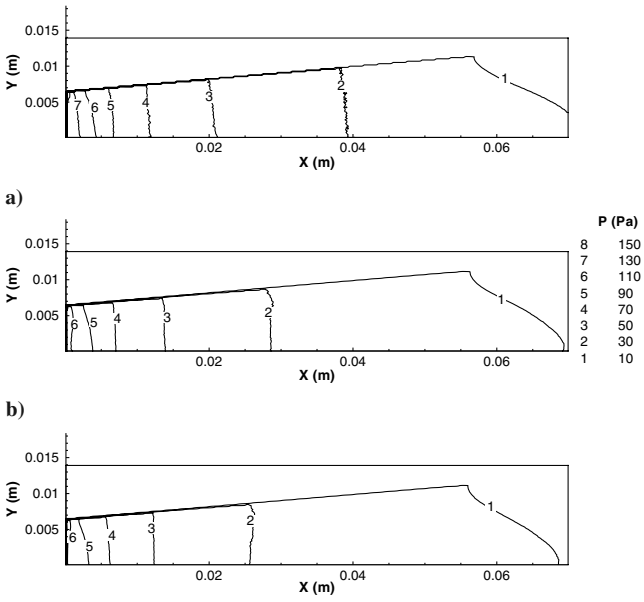

Fig. 3 Ethanol gas pressure without condensation: a) case 1, b) case 2, and c) case 3.

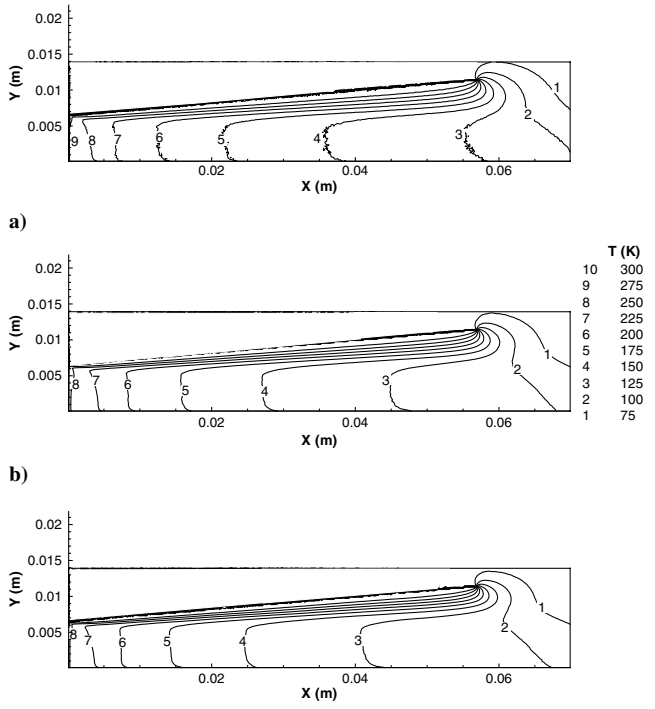

Fig. 4 Ethanol gas temperature without condensation: a) case 1, b) case 2, and c) case 3.

that the condensation results for cases 2 and 3 will be similar, with the onset of condensation closer to the throat than in case 1.

2. Condensation Results: Case 1

Case 1, which contains pure ethanol, was simulated with condensation. The condensation processes described in Sec. II were incorporated into the DSMC code to simulate cluster formation and growth in the flow. Figure 8a shows the contours of the ethanol gas number density in the flowfield for the case 1 simulations with and without condensation. The condensation result begins to deviate significantly from the noncondensation result about one-third of the way down the axis, and the deviation becomes continuously more pronounced at longer axial distances. The results show that the ethanol gas molecules are being consumed by condensation and that the amount of gas consumed increases as the flow moves downstream.

Because the ethanol gas is the source of ethanol clusters, as the gas number density decreases, the cluster number density increases, as shown in Fig. 9. Figure 9 shows the cluster number density along the nozzle centerline, with condensation onset occurring at about $x = 0.016$ m. The number density then increases rapidly as the ethanol clusters are formed through the process of nucleation. The cluster number density reaches a maximum value of about 6×10^{18} clusters per cubic meter. After this peak concentration, the flow conditions are such that no further nucleation occurs. The clusters continue to evaporate and coalesce and the flow continues to expand, resulting in a slight decrease in cluster number density toward the nozzle exit.

Another important characteristic of the condensation in the flow is the cluster size. The average cluster size on the nozzle centerline is

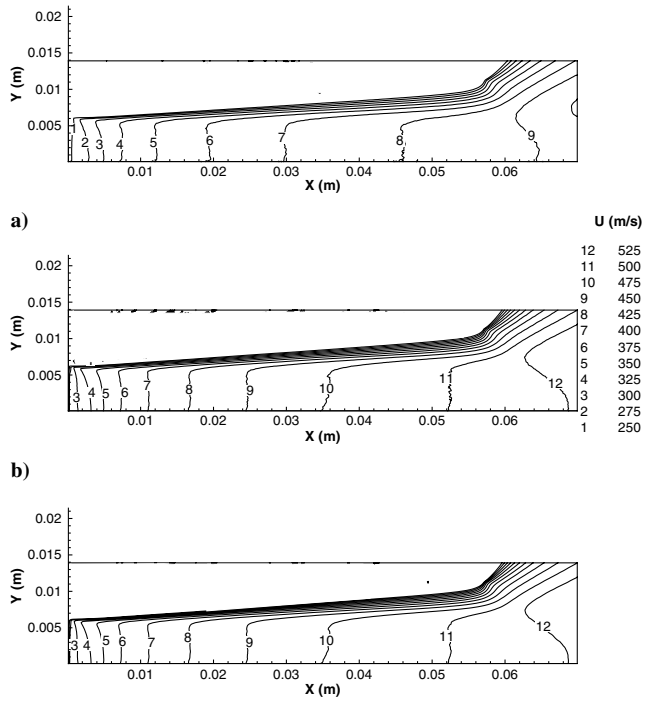

Fig. 5 Ethanol gas *x* velocity without condensation: a) case 1, b) case 2, and c) case 3.

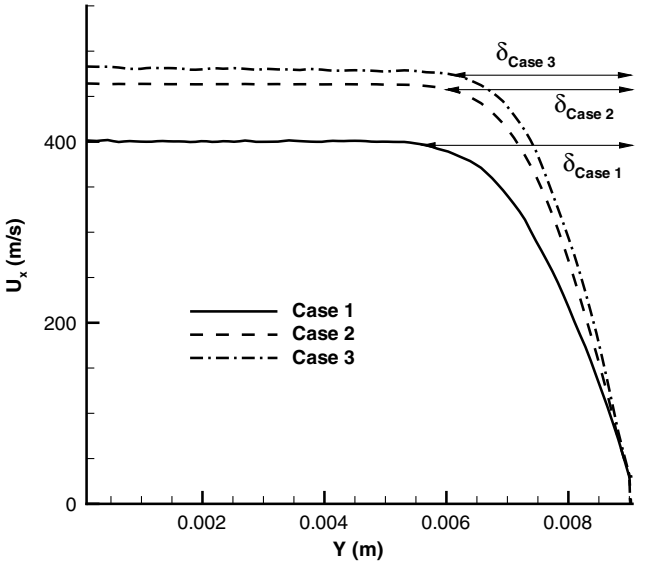

a) Near nozzle center (x=0.03 m)

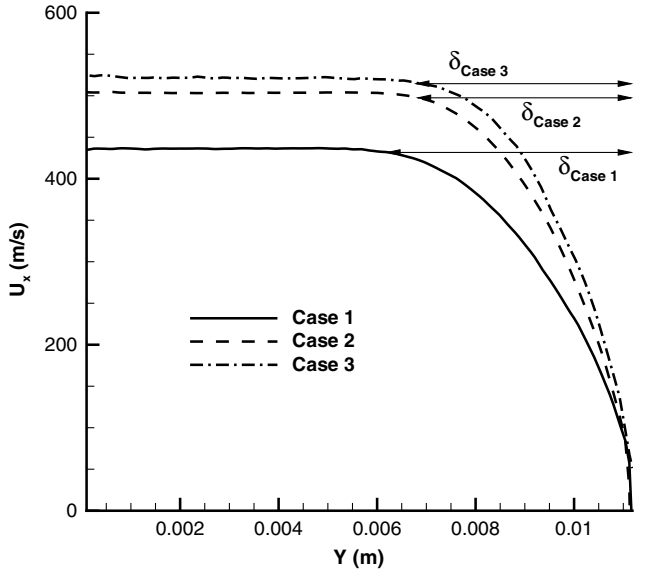

b) Near nozzle exit (x=0.055 m)

Fig. 6 Ethanol gas *x* velocity profile and velocity boundary-layer thickness for cases 1–3 without condensation.

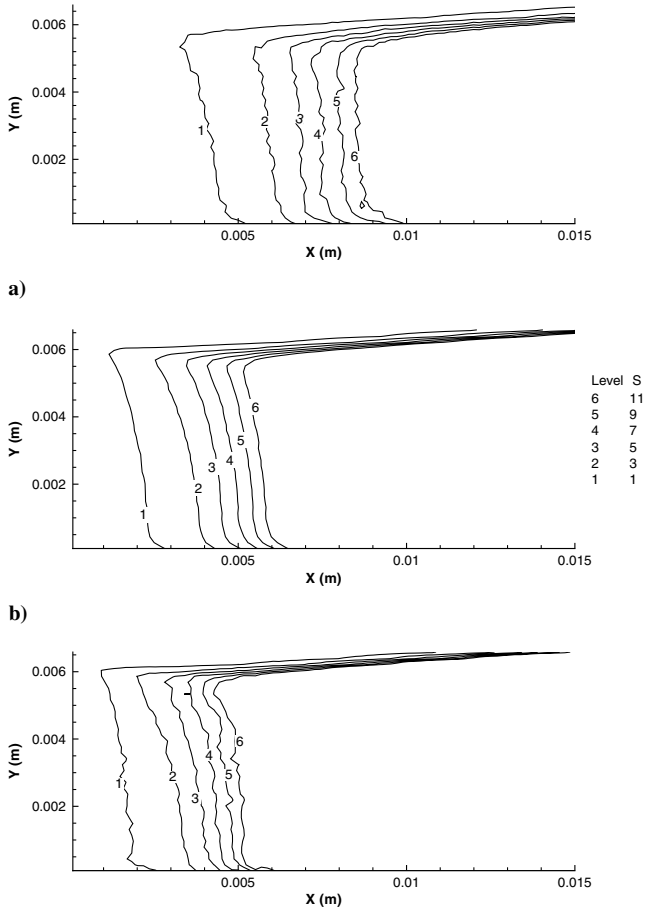

Fig. 7 Degree of supersaturation near the nozzle throat without condensation: a) case 1, b) case 2, and c) case 3.

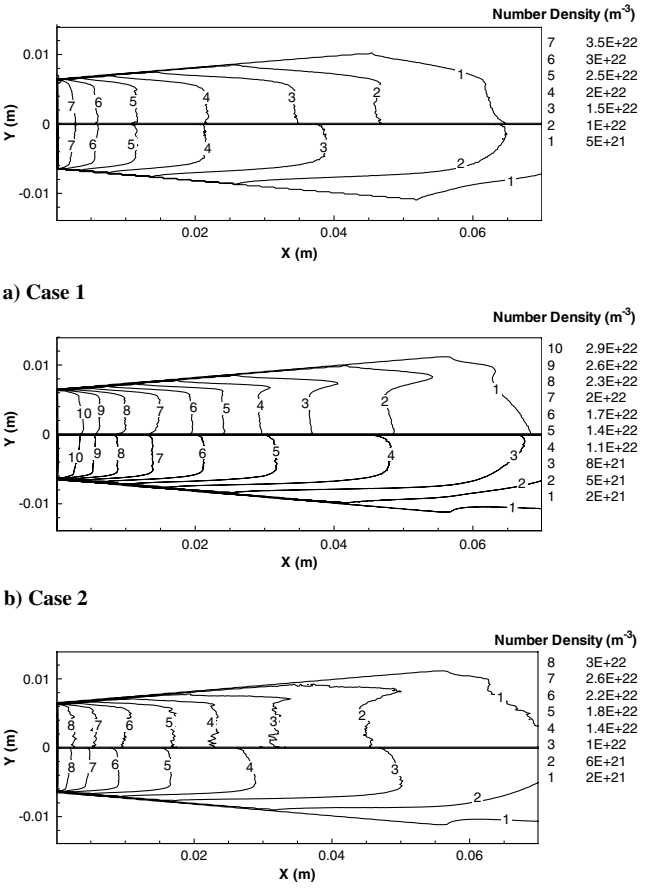

Fig. 8 Ethanol gas number density: a) and b) with condensation, and c) without condensation.

shown in Fig. 10. The cluster size is quite small near the point of condensation onset and increases monotonically to a value of about 1950 at the nozzle exit. Cluster size is affected by the processes of condensation, evaporation, and coalescence. Each cluster that forms through nucleation is introduced to the computational domain at the critical cluster size determined by classical nucleation theory (see Sec. II.B). As it travels through the flow, a cluster can collide with condensible gas particles and grow through condensation. In this work, it is assumed that ethanol has a sticking probability of unity,[§] meaning that any time an ethanol gas particle collides with a cluster, condensation occurs. Condensation allows clusters to grow much larger than their initial size. In addition to condensation, the clusters can collide with each other and merge into a single, larger cluster through coalescence. This occurs more frequently in areas with large clusters or high cluster number densities. A cluster can also shrink through evaporation depending on the individual cluster and local gas conditions. A comparison of the case 1 curve with cases 2–5 is provided later.

The cluster mass fraction is defined as the mass of ethanol clusters divided by the total ethanol mass so that a value of zero indicates no condensation and a value of 1.0 indicates that all of the ethanol in the flow has condensed to form clusters. Combining the previous two results for cluster number density and size, the cluster mass fraction can be calculated. Experimental results for the cluster mass fraction are provided, and so the simulation and experimental results can be compared as shown in Fig. 11. The experimental values and associated approximate error bars are adapted from a figure in the original experimental paper [8]. The cluster formation in the simulation results is shifted downstream of the experimental condensation onset point. In addition, the experimental curve has a larger slope, indicating that the ethanol gas is consumed more quickly in the experiment than in the simulation. The experimental result levels off to a value of about 0.95 approximately two-thirds of the way down the nozzle, whereas the simulation result is still increasing at the nozzle exit.

Another way to interpret the condensation in a flow is to look at the mass and energy conservation inside the nozzle. Figure 12a shows the mass flow rate for case 1, with the total mass flow rate constant from the nozzle throat to the exit, as expected. Near the throat, all the

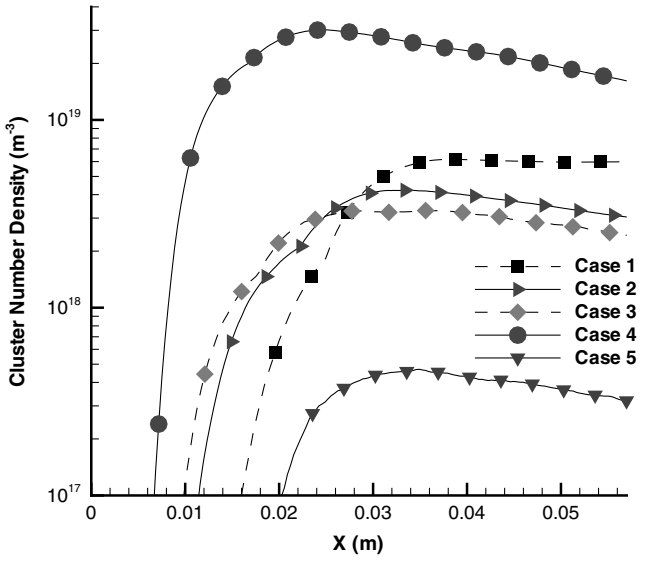

Fig. 9 Ethanol cluster number density on the nozzle centerline.

[§]Wyslouzil, B., private communication from February 2007.

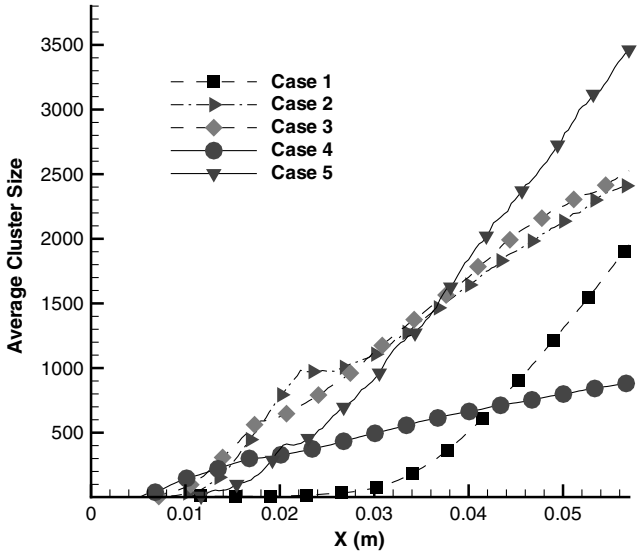

Fig. 10 Average size of ethanol clusters on the nozzle centerline.

mass is in the gaseous state. As the axial distance increases, condensation begins and the cluster mass flow rate increases. At the nozzle exit, the clusters account for one-third of the total mass flow rate. Figure 13a shows that all the energy flow is also in the gas near the nozzle throat. Downstream, the energy flow rate of the clusters increases very little, contributing only approximately 5% of the total energy flow rate at the nozzle exit. The ethanol gas energy flow rate remains dominant even as the cluster number density and size increase because the gas has a much higher kinetic energy than the clusters. Although the gas and cluster particles have similar axial velocities, on average the gas particles have a much larger radial velocity component than the clusters. These large radial velocities are approximately evenly distributed in the positive and negative directions so that the net flow is in the axial direction, but the average radial velocity magnitude of the gas particles is on the order of the average axial velocity. Therefore, the kinetic energy of the gas, which is based on the velocity magnitude, is much larger for the gas than for the clusters. This results in a much larger contribution to the total energy flow rate from the gas than from the clusters. The total energy flow rate is nearly constant from the throat to the exit. As the contribution from the clusters increases, a small error is introduced. However, the standard deviation of the total energy flow rate is only about 0.5% of the mean.

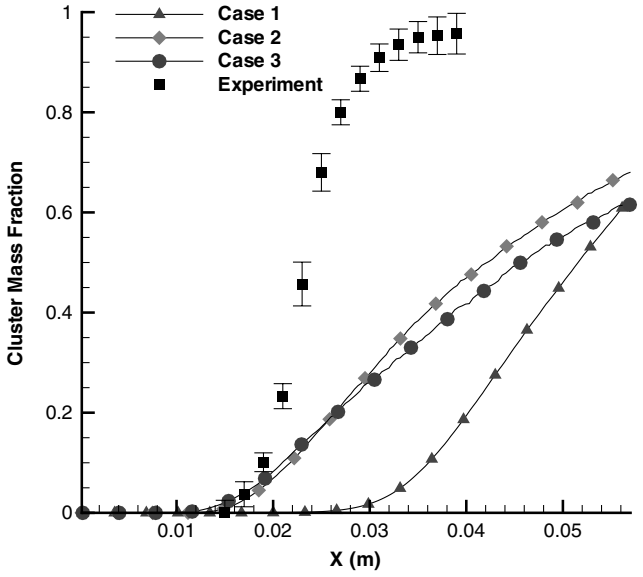

Fig. 11 Mass fraction of ethanol clusters on the nozzle centerline for cases 1–3.

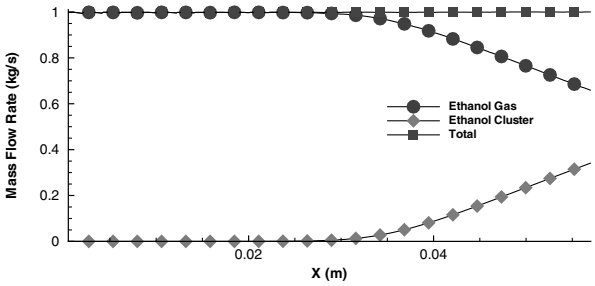

a) Case 1 (normalized by mass flow rate at nozzle exit = 9.1 x 10^{-5} kg/s)

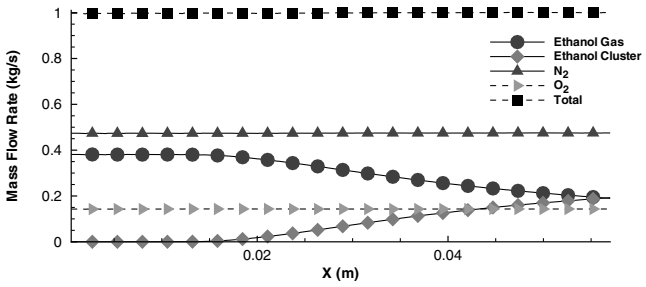

b) Case 2 (normalized by mass flow rate at nozzle exit = 2.4 x 10^{-4} kg/s)

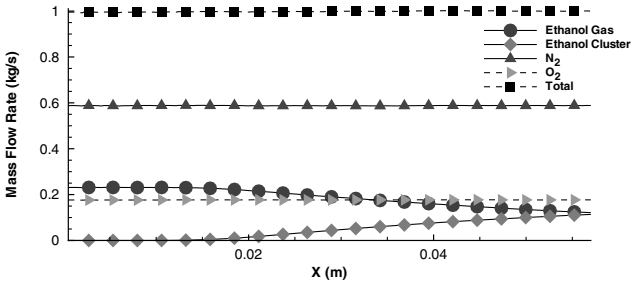

c) Case 3 (normalized by mass flow rate at nozzle exit = 4.0 x 10^{-4} kg/s)

Fig. 12 Comparison of gas and cluster mass flow rates for cases 1–3.

3. Impact of Nucleation and Evaporation Models

The simulation of homogeneous condensation depends on the various physical models selected. In particular, previous works [6,19] have shown that the solutions of the condensation flow are sensitive to the nucleation model. To help assess the accuracy of the solutions, the sensitivity of the results to the nucleation model can be evaluated. The nucleation rate equation given by classical nucleation theory was discussed in Sec. II.B. The nucleation rate is dependent on the surface tension. The surface tension is described by an equation given in Table 2, which is a function of the temperature. The nucleation rate is a function of the temperature and pressure, so that by holding the pressure constant, one can evaluate the relationship between the nucleation rate and surface tension. Figure 14 shows the nucleation rate as a function of the surface tension for pressures between 40 and 45 Pa. It is clear that the nucleation rate, shown on a logarithmic scale, is very sensitive to the surface tension. Because the surface tension equation is a curve fit based on experimental data, small errors are possible that could significantly impact the nucleation rate.

In addition, the nucleation rate equation could be inaccurate. Recent experimental research [20] has led to the development of a correction to the classical nucleation rate for water. DSMC simulations of condensation in a supersonic plume using both the classical nucleation rate and the corrected nucleation rate have shown that the condensation results are sensitive to the choice of nucleation rate [19]. No such correction exists presently for the ethanol nucleation rate, but it is possible that there is a discrepancy between the nucleation rate given by CNT and the actual value in the case of ethanol, as there is for water. Therefore, the sensitivity of the results to the nucleation rate is evaluated. Figure 15 shows the impact on the

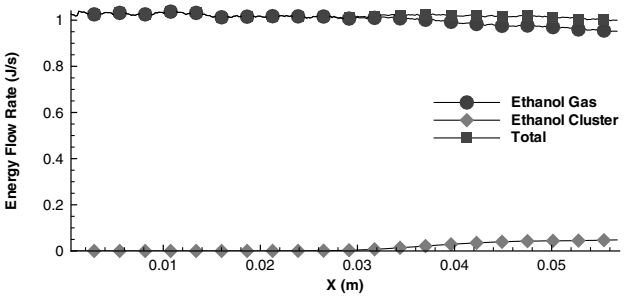

a) Case 1 (normalized by energy flow rate at nozzle exit = 18.5 J/s)

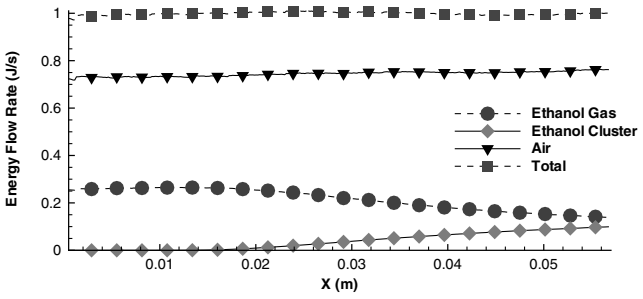

b) Case 2 (normalized by energy flow rate at nozzle exit = 77.0 J/s)

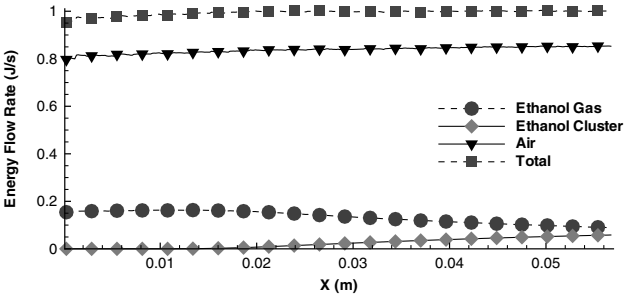

c) Case 3 (normalized by energy flow rate at nozzle exit = 125.7 J/s)

Fig. 13 Comparison of gas and cluster energy flow rates for cases 1–3.

simulated cluster mass fraction obtained by multiplying the nucleation rate by a constant value. The result from Fig. 11 is included and is denoted by a multiplier value of 1.0. It can be seen that a constant multiplier less than 1.0 results in a lower cluster mass fraction and that larger multipliers increase the cluster mass fraction. These multipliers have a significant impact on the results, and a multiplier of 100.0 brings the results very close to the experimental values. Based on the sensitivity of the nucleation rate to the surface tension and the uncertainty in the CNT nucleation model, it is possible that future improvements to the nucleation model may help improve the agreement between simulations and measurements.

Another model that impacts the simulation results is the evaporation model. As discussed in Sec. II.B, the evaporation rate is derived by assuming that a cluster's evaporation rate is equal to its condensation rate in a vapor environment and that the cluster size is equal to the critical size of that vapor environment. Figure 16 shows cluster mass fraction results for case 1 with and without the evaporation process activated. The figure shows that the evaporation process has a significant impact on the total amount of condensation. Figure 17 shows the average cluster size on the nozzle centerline for case 1 with and without evaporation. The shapes of the two curves are very similar, but when evaporation is active, the curve appears to shift downstream. Knowing that the point of condensation onset must be the same in both cases, one can conclude that the evaporation plays a large role in the region immediately downstream of the onset point and slows the cluster growth. Note that, although the average cluster size in the case with evaporation is monotonically increasing from the onset location to the exit, the average cluster size in the case

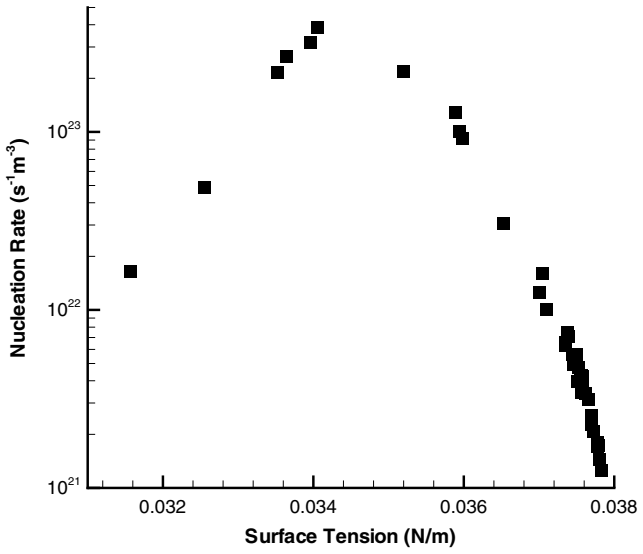

Fig. 14 Nucleation rate as a function of surface tension with pressure held constant.

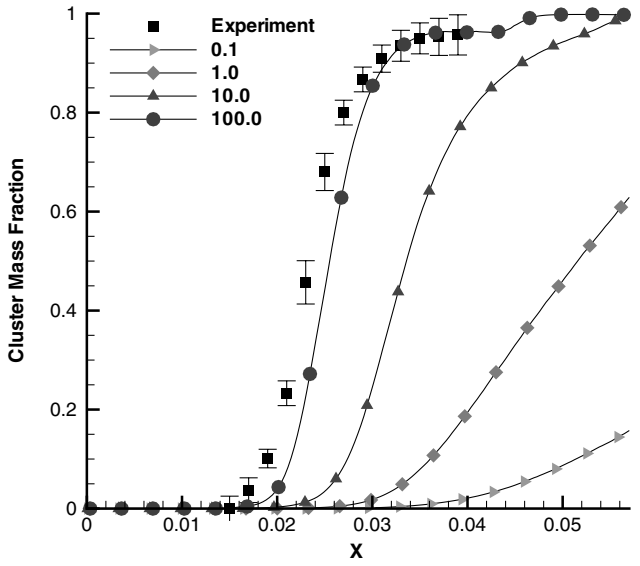

Fig. 15 Impact of artificially adjusting the nucleation rate by a constant multiplier for case 1.

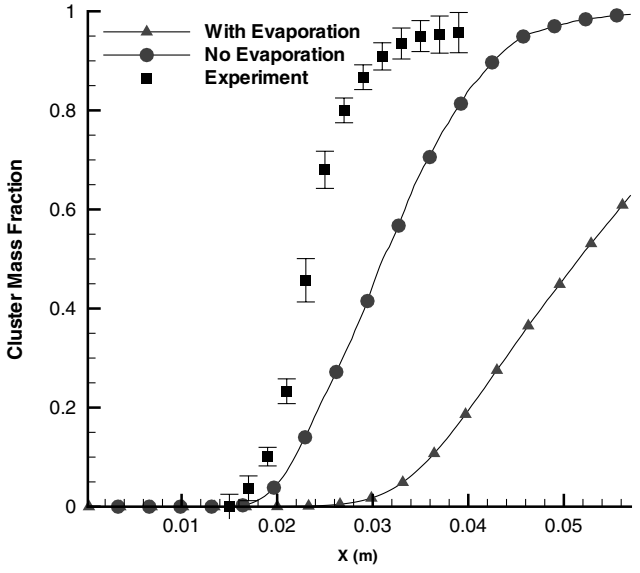

Fig. 16 Impact of the evaporation process on the cluster mass fraction for case 1.

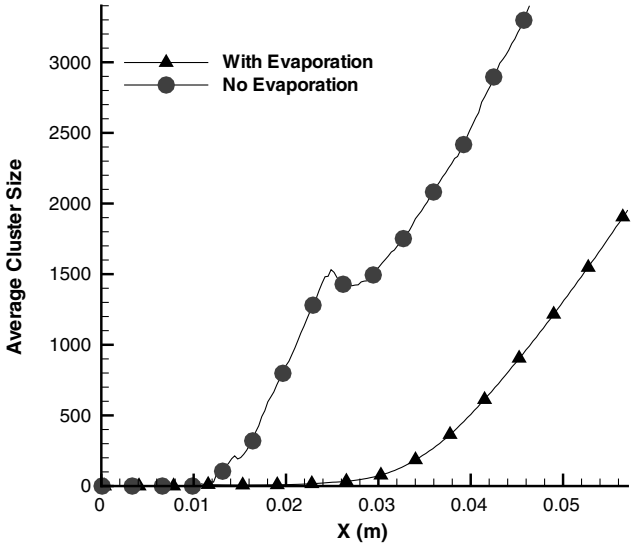

Fig. 17 Impact of the evaporation process on the average cluster size for case 1.

without evaporation decreases slightly near $x = 0.014$ and 0.024 m before increasing further. This is a result of the saturation pressure equation. The saturation pressure is expressed by three equations for three temperature regimes, as given in Table 2. When the temperature reaches a boundary between two of these equations, there is a slight discontinuity in the saturation pressure, which causes a small increase in the nucleation rate and a corresponding drop in average cluster size. This effect is not noticeable in regions where the evaporation process plays a prominent role, as seen in Fig. 17. Even in cases in which this kink in the average cluster size curve is visible, the effect on the cluster mass fraction is negligible, as seen in Fig. 16.

From Figs. 16 and 17, one can see that the choice of evaporation model also has a significant impact on the results. Many factors influence the results, and even though removal of the evaporation process brings the simulation result closer to the experimental result in this case, one cannot conclude that removing the evaporation process entirely would give the best agreement with the experiment. When other factors have been considered, this may actually result in an overestimate of the cluster mass fraction. One can only conclude from these results that the simulation is sensitive to the evaporation process. Other evaporation models exist, such as the Rice–Ramsberger–Kassel model [21], and an improvement in the evaporation model could be beneficial to improving the simulation.

4. *Condensation Results: Cases 2 and 3*

In cases 2 and 3, air is added to the simulation along with ethanol. The air is assumed to be free of water vapor and is modeled as 79% N_2 and 21% O_2. Because at the simulation conditions dry air would not condense, the air is treated as a noncondensible, inert gas. An N_2 or O_2 monomer can interact with other N_2, O_2, or ethanol monomers through monomer–monomer collisions, as described in Sec. II.C.1. They can also interact with ethanol clusters through nonsticking collisions, as described in Sec. II.C.2. The air monomers can exchange energy with ethanol clusters through these collisions, but they cannot add mass to the clusters or remove mass from them. As mentioned, the air monomers also are assumed to refrain from forming clusters of their own.

Figure 8b shows the ethanol gas number density in the nozzle for case 2 with and without condensation. As for case 1, one can see that the presence of condensation causes the number density at a given axial location to decrease. This occurs because the ethanol clusters consume the ethanol gas through the condensation process. The impact of the condensation becomes more pronounced for larger axial locations. In the condensation case, it can also be seen that there is a larger decrease in the number density near the nozzle axis, showing that the majority of the condensation occurs in the core of the flow where the pressure is higher.

Figure 12b shows the mass conservation for case 2. It is clear that the mass flow rates for the N_2 and O_2, as well as the total mass flow rate, remain constant along the length of the nozzle. For the ethanol, the gas mass flow dominates near the throat where condensation has not yet begun. By the nozzle exit, however, the contributions from the ethanol gas and the clusters are approximately equal. This indicates that a significant portion of the ethanol gas has condensed into clusters.

With regard to energy conservation for case 2, similar results can be seen in Fig. 13b. The total energy flow rate is approximately constant along the nozzle axis. The energy flow rate of the gas is also approximately constant but increases slightly from throat to exit. This indicates that the air is gaining some energy from the ethanol through the collision process. As with the mass, the ethanol gas energy flow rate dominates over the cluster flow rate near the nozzle throat. Near the nozzle exit, the contributions from the ethanol gas and the clusters are quite close, although the ethanol gas energy flow rate remains larger than that of the clusters.

Figure 8c shows the ethanol gas number density for case 3 with and without condensation. In case 3, the amount of air is increased to a mole fraction of 0.84. As in case 2, the ethanol gas number density decreases due to condensation. Figures 12c and 13c show the mass and energy conservation for case 3. The results are very similar to those for case 2, except that the values for air have approximately doubled. Comparing the results for cases 1–3 in Fig. 12, it can be seen that at the nozzle exit about one-third of the ethanol has condensed in case 1, but about one-half of the ethanol has condensed in cases 2 and 3, indicating that the addition of air to the simulation increases the total amount of condensation.

Figure 9 provides a comparison of the cluster number density along the nozzle centerline for cases 1 (no air), 2 (low air), and 3 (high air). The curves for the three cases have a similar shape. In each case, the number density increases from zero at the throat to a peak value near the midpoint of the nozzle axis. The number density then decreases from this peak point to the nozzle exit. The increasing number density indicates that new clusters are forming. After the number density reaches its peak, nucleation ceases and the number density along the centerline decreases as expansion continues and clusters continue to be consumed by evaporation and coalescence.

A comparison of the curves for cases 1–3 in Fig. 9 shows that, as the amount of air is increased, the axial location of the condensation onset shifts toward the nozzle throat. From the onset point, the cluster number density increases at approximately the same rate in all three cases. However, the peak value of the cluster number density is dependent on the amount of air; the maximum value of the cluster number density decreases as the amount of air increases. In the region between the number density peak and the nozzle exit, the cluster number density decreases in all three cases, but the decrease is more rapid in the cases in which air is included. This more rapid decrease in the cluster number density toward the end of the nozzle is indicative of the faster expansion and smaller boundary layer seen in cases 2 and 3 and discussed in reference to the noncondensation results in Sec. III.B.1 and Fig. 5. These results indicate that the faster expansion in the cases with air results in an earlier condensation onset point and a smaller nucleation region than in case 1. It is also clear from Fig. 9 that cases 2 and 3 are more similar to each other than to case 1, as predicted from the noncondensation results in Sec. III.B.1.

In Fig. 10, one can again see the similarity between cases 2 and 3. Figure 10 shows the average cluster size on the nozzle centerline for cases 1–3. In all three cases, the average cluster size increases as the axial distance from the throat increases. This is consistent with CNT, which states that clusters above the critical size tend to grow in a supersaturated vapor environment. The average cluster size results are very similar for cases 2 and 3, whereas significant differences are seen in the results for case 1. First, it has already been discussed that condensation begins closer to the nozzle throat in cases 2 and 3 than in case 1, and so the downstream shift of the case 1 curve is expected. Near their respective onset points, the rate of size increase is much higher for cases 2 and 3 than for case 1. As discussed in Sec. II.B, the evaporation process plays an important role in this region for case 1, slowing the cluster growth process considerably. The results in

Fig. 10 indicate that the presence of air decreases the impact of the evaporation process, causing faster growth in this region in cases 2 and 3. Note that there is a small kink in the average cluster size curve at $x = 0.018$ m in case 2 and at $x = 0.022$ m in case 3. This is again a result of discontinuities in the saturation pressure curve, as discussed in Sec. II.B, and their impact on the cluster mass fraction is negligible. As the flow moves farther from the onset point into the region where evaporation is no longer dominant, the rate of size increase in case 1 becomes larger than that of cases 2 and 3. This discrepancy results from the fact that, when air is present, nonsticking collisions occur between air monomers and clusters. The probability of having a cluster–monomer collision that does not result in cluster growth is greatly increased. This results in a decrease in the cluster growth rate in cases 2 and 3 as compared with case 1.

Figure 11 shows the cluster mass fraction for cases 1–3, which incorporates both the cluster number density and the average cluster size. The same trends seen in Figs. 9 and 10 can be observed here. Cases 2 and 3 are more similar to each other than to case 1, indicating that the presence of air has an important impact on the condensation. The condensation onset occurs closer to the nozzle throat in cases 2 and 3. The condensation onset point will be discussed in depth in Sec. III.D. The cluster mass fraction is larger in cases 2 and 3 at most points along the axis, but near the nozzle exit, the three cases approach a similar value of the cluster mass fraction. Although cases 2 and 3 have similar results, there is a difference between them that grows with the axial distance from the throat. This is the result of differences in the flowfields of the two cases that occur because of the amount of air impacts the boundary layer inside the nozzle. However, this difference is much smaller than the difference between cases 1 and 2. Figure 11 also includes the experimental results for the cluster mass fraction. The experiment differs from the simulations in that a much larger amount of air was used in the experiment. The results for cases 2 and 3 show better agreement with the experiment than case 1, both in the condensation onset point and in the value of the cluster mass fraction along the nozzle axis. These results indicate that the addition of air to the simulation can improve results, even if the full amount of air used in the experiment cannot be simulated.

The results still show a large difference in the cluster mass fraction between the simulation and the experiment. These results could be improved with changes to the nucleation rate, as discussed in Sec. III.B.3. As in Sec. III.B.3, the nucleation rate can be artificially increased to assess the sensitivity of the results to the nucleation rate. Figure 18 shows the impact on the cluster mass fraction result from case 3 of multiplying the nucleation rate by a constant factor. One can see that increasing the nucleation rate by a factor of 10.0 increases the cluster mass fraction significantly. With a multiplier of 100.0, the shape of the cluster mass fraction curve is quite similar to that of the experimental curve. Although the condensation onset point of the simulation result is closer to the throat of the nozzle, the agreement between the simulation and the experiment is very good at axial distances greater than 0.03 m. These results support the conclusion made in Sec. III.B.3 that future modifications to the calculation of the nucleation rate could significantly improve agreement between simulation and experimental results.

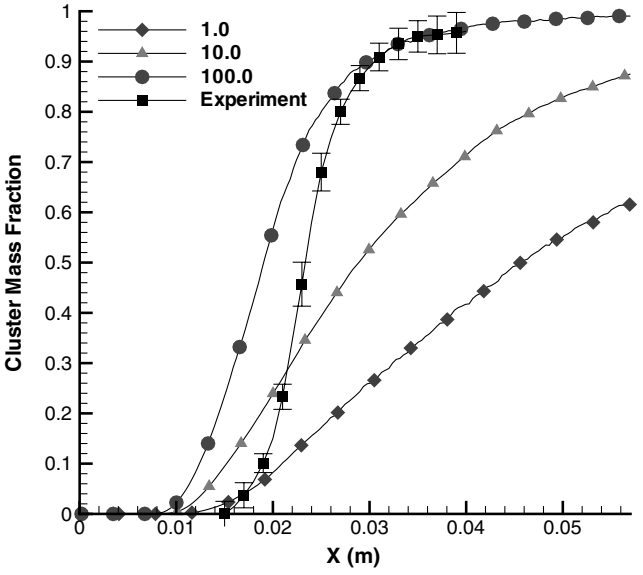

Fig. 18 Impact of artificially adjusting the nucleation rate by a constant multiplier for case 3.

C. Results: Cases 4 and 5

Cases 4 and 5 are studied to assess the ability to simulate different amounts of ethanol. As with cases 1–3, cases 4 and 5 are based on experiments by Wegener et al. [8]. There are three experimental cases presented in the work of Wegener et al., each corresponding to the different mass fraction amounts of ethanol used. The numerical simulations of the first experimental case have been shown in simulation cases 1–3. The other two experimental cases are studied in this section. In the experimental case that corresponds to simulation cases 1–3, the mass fraction of ethanol was 0.005. The experimental case that corresponds to simulation case 4 had a higher ethanol mass fraction of 0.008, whereas the experimental case that corresponds to simulation case 5 had a lower ethanol mass fraction of 0.0034. Details of the experimental conditions can be found in Table 1. In cases 4 and 5, as in cases 1–3, the same partial pressure of ethanol gas was used in the simulation as was used in the experiment. It has been shown in Sec. III.B.4 that the simulation results improve when some air is added to the simulation, although the full amount of air used in the experiments cannot be simulated in DSMC. Therefore, the same amount of air was used in cases 4 and 5 as was used for case 3.

The cluster number density along the nozzle centerline is shown in Fig. 9. The results for cases 4 and 5 are similar to those seen in cases 1–3. The condensation process begins near the nozzle throat, where the cluster number density becomes greater than zero. The cluster number density then increases rapidly through the nucleation process until it reaches a peak value at an axial distance from the throat of about 0.022 m in case 4 and 0.034 m in case 5. The cluster number density then decreases as the nucleation region ends and the flow continues to expand to the nozzle exit. Comparing cases 3–5, one can see that the cluster number density decreases as the amount of ethanol in the simulation decreases. In fact, the peak value of the number density in case 5 is almost 2 orders of magnitude lower than that of case 4. This indicates that, as the partial pressure of ethanol in the simulation increases, the nucleation rate increases, which is consistent with the CNT nucleation rate given in Eq. (5).

The average cluster size on the nozzle centerline is shown in Fig. 10. The maximum value of average cluster size, which occurs at the nozzle exit, is about 900 in case 4 and about 3500 in case 5. The average cluster size increases approximately linearly from the condensation onset point to the nozzle exit, as in case 3. The rate of cluster size increase is larger for smaller amounts of ethanol.

In Fig. 19, the cluster mass fraction for case 4 is compared with the corresponding experimental result. The simulation result shows good agreement with the experimental result near the condensation onset point. As the axial distance from the throat increases, the simulation result deviates more from the experimental result. The value of the cluster mass fraction given by the simulation is lower than the value given by the experiment at all points along the axis. This is the same trend seen in case 3. Both the experiment and the simulation reach a maximum value of the cluster mass fraction of about 0.9, meaning that 90% of the ethanol condenses to form clusters.

In Fig. 20, the cluster mass fraction for case 5 is compared with the experimental data. It can be seen that the results from the simulation and the experiment are similar near the condensation onset point but deviate significantly as the axial distance from the throat increases. In the experiment, all the ethanol had condensed by the nozzle exit, whereas in the simulation only about 20% of the ethanol condenses. Comparing the result for case 3 in Fig. 11 with Figs. 19 and 20, one can see that the agreement with the experimental results improves as the partial pressure of ethanol increases. Note that the simulation

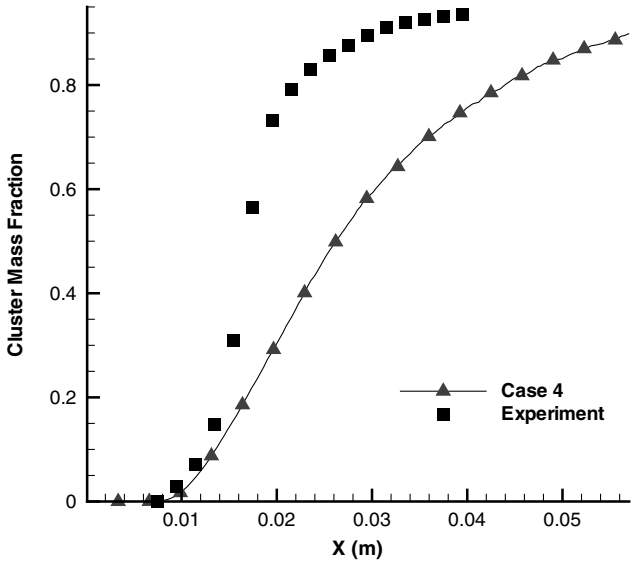

Fig. 19 Mass fraction of ethanol clusters on the nozzle centerline for case 4.

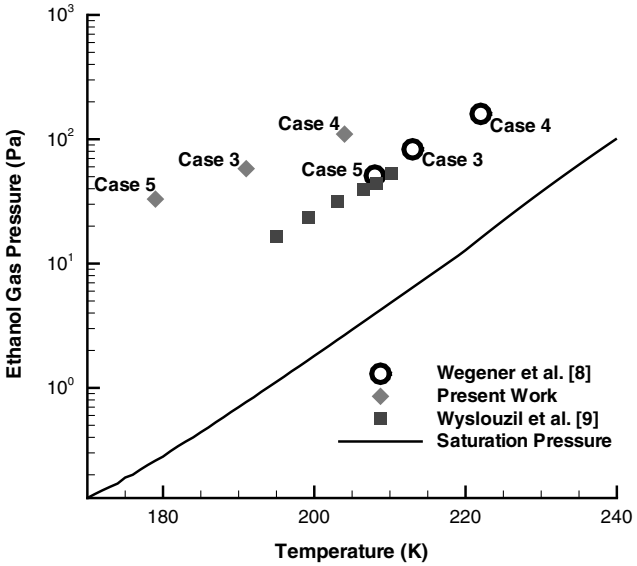

Fig. 21 Comparison of condensation onset point for cases 3–5 with experimental results [8,9].

results are basically independent of the amount of air, as discussed in Sec. III.B.4. Therefore, it can be concluded that the nucleation rate, which is directly proportional to the partial pressure of the condensible gas, is the most likely reason for the increased discrepancy between the experimental and simulation results as the partial pressure of ethanol decreases. It may be possible to improve the agreement between the simulation and the experiment for cases with lower partial pressures of condensible gas by improving the nucleation rate model.

D. Condensation Onset

The condensation onset point in ethanol has been measured in many experiments using different methods, including supersonic nozzles and diffusion cloud chambers [8–11]. The condensation onset point is given in terms of the temperature and condensible gas pressure and can be determined by different measurements, including the deviation in static pressure or temperature from the isentrope [8,9,14] and an increase in the intensity of scattered light [10,11]. In this work, the onset point is defined as the point at which the condensed mass fraction reaches 1.0×10^{-4}, as in Wegener et al. [8].

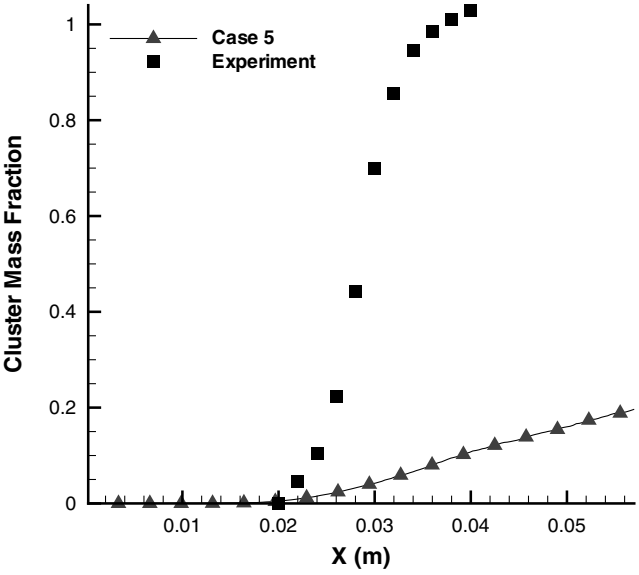

Fig. 20 Mass fraction of ethanol clusters on the nozzle centerline for case 5.

In [8], the experimental results of Wegener et al. are compared with several other sets of experimental data. The data show that there is significant variation in the onset point. However, all the results fall in the supersaturated region, where the condensible gas pressure at condensation onset is higher than the saturation pressure at a particular temperature. In addition, the results show that the onset and saturation pressures have a similar temperature dependence.

The condensation onset points for cases 3–5 are compared with the results from the corresponding experiments in Fig. 21. Figure 21 also shows the experimental results of Wyslouzil et al. [9] for condensation onset in ethanol in a supersonic nozzle. (Wyslouzil et al. [9] consider binary condensation in ethanol propanol and ethanol water. In this work, only the results for the pure ethanol cases are included.) Both sets of experimental results and the simulation results show a similar relationship between the temperature and pressure at the onset point as is seen in the saturation pressure curve for ethanol. In all three sets of results, there is also an increase in temperature and pressure at onset as the partial pressure of ethanol gas is increased. Comparing the onset points from the simulations with the experimental results of Wegener et al. [8] for cases 3–5, one can see that, for a given temperature, the onset occurs at a higher pressure in the simulation than in the experiment. Similarly, if the pressure is held constant, the onset temperature is lower in the simulation than in the experiment. This places the simulation onset points farther from the saturation pressure curve, at a higher degree of supersaturation, than the experimental results. This indicates that condensation occurs more readily in the experiments than in the simulations. However, an examination of other sets of experimental data [8] show that there is some variation in the onset points given by different experiments. Other data sets show onset points both closer to and farther from the saturation line than the results given by Wegener et al. This variation may result from the fact that there are several different ways to define the condensation onset point, as already discussed. Therefore, although the simulation onset points and the experimental onset points of Wegener et al. differ, the difference is similar to the variation between different sets of experimental results, and so it can be concluded that the simulation results give a good approximation to the condensation onset point.

IV. Conclusions

In this work, the DSMC method has been applied to simulate the homogeneous condensation of ethanol in a supersonic nozzle flow. CNT was used to calculate the nucleation rate, and models were developed for all the processes involved in the formation and growth of clusters, including nucleation, evaporation, and monomer–

monomer, cluster–cluster, and cluster–monomer collisions, both sticking and nonsticking.

Simulation results were presented for flow without condensation. Three cases were presented with a constant amount of ethanol and an increasing amount of carrier gas in the simulation. It was shown that the addition of the carrier gas caused a significant change in the flowfield, but that the change in the flowfield was not proportional to the amount of carrier gas. Doubling the amount of carrier gas caused only a small change in the flowfield compared with the initial addition of the carrier gas. The results also showed that the addition of the carrier gas caused the degree of supersaturation near the nozzle throat to increase.

Results were then presented for the flow with condensation. Again, increasing amounts of carrier gas were added to the simulation to assess the impact of the carrier gas on cluster formation and growth. As predicted by the noncondensation results, the point of condensation onset moved closer to the throat when air was added, and the results for two cases that included the carrier gas were more similar to each other than to the case in which the carrier gas was omitted. This suggests that a reasonable result can be obtained using a small amount of carrier gas, because the high carrier gas pressures often used in experiments cannot be simulated in DSMC.

Finally, results for the point of condensation onset were compared with the experimental data. The simulation results show good agreement with the experimental data. In both the experimental and simulation results, the onset point lies at a pressure higher than the ethanol saturation pressure at the onset temperature, indicating that, as discussed, condensation occurs where the flow is in the supersaturated state. Both the experimental and simulation results show that the temperature and pressure of the onset point increase as the partial pressure of the ethanol gas is increased.

Several steps can be taken in the future to improve the results presented in this work. One is to improve the nucleation rate model. The CNT rate used in this work has previously been shown to be in need of a correction factor in the case of water. In addition, the CNT rate is derived with the assumption that the nucleation process has little impact on the vapor number density. Given the large amount of condensation seen in the simulations in this work, this assumption may not be valid in this case. It has been shown that results are sensitive to the nucleation rate, and so an improved nucleation rate model could lead to an improvement in the simulation results.

In addition, it has been shown that the simulation results are sensitive to the evaporation model. In the simulations presented in this work, evaporation has a significant impact on the cluster growth process, particularly in the region close to the condensation onset point. Therefore, the choice of the evaporation model is important to the simulation results. In the future, the evaporation model should be considered more closely and the inclusion of a better model should be considered.

Acknowledgments

The research performed at the Pennsylvania State University was supported by the Air Force Office of Scientific Research grant F49620-02-1-0104, whose support is gratefully acknowledged. Special thanks also go to M. Ivanov of the Institute of Theoretical and Applied Mechanics, Russia, for the use of the original SMILE code.

References

[1] Rebrov, S., and Gerasimov, Y., "Investigation of the Contamination Properties of Bipropellant Thrusters," AIAA Paper 2001-2818, 2001.

[2] Prikhodko, V., Chekmarev, S., Yarygin, V., and Yarygin, I., "Rise of a Near-Wall Liquid Film over the Outer Surface of a Nozzle Accompanying Supersonic Gas Flow into Vacuum," *Doklady Physics*, Vol. 49, No. 2, 2004, pp. 119–212. doi:10.1134/1.1686884

[3] Ivanov, M., Khotyanovsky, D., Kudryavtsev, A., Vashchenkov, P., Markelov, G., and Schmidt, A., "Numerical Study of Backflow for Nozzle Plumes Expanding into Vacuum," AIAA Paper 2004-2687, 2004.

[4] Alexeenko, A., Wadsworth, D., Gimelshein, S., and Ketsdever, A., "Numerical Modeling of ISS Thruster Plume Induced Contamination Environment," *Proceedings of SPIE: The International Society for Optical Engineering*, Vol. 5526, 2004, pp. 125–136. doi:10.1117/12.559059

[5] Bird, G., *Molecular Gas Dynamics and the Direct Simulation of Gas Flows*, Clarendon Press, Oxford, 1994.

[6] Zhong, J., "The Modeling of Homogeneous Condensation in Free-Expanding Plumes with the Direct Simulation Monte Carlo Method," Ph.D. Thesis, Pennsylvania State University, University Park, PA, 2005.

[7] Yarygin, V., Prikhodko, V., Yarygin, I., Gerasimov, Y., and Krylov, A., "Gas-Dynamic Aspects of the Contamination Problem at the International Space Station 1. Model Experiments," *Thermophysics and Aerodynamics*, Vol. 10, No. 2, 2003, pp. 269–286.

[8] Wegener, P. P., Clumpner, J. A., and Wu, B. J. C., "Homogeneous Nucleation and Growth of Ethanol Drops in Supersonic Flow," *Physics of Fluids*, Vol. 15, No. 11, Nov. 1972, pp. 1869–1876. doi:10.1063/1.1693796

[9] Wyslouzil, B., Heath, C., and Cheung, J., "Binary Condensation in a Supersonic Nozzle," *Journal of Chemical Physics*, Vol. 113, No. 17, Nov. 2000, pp. 7317–7329. doi:10.1063/1.1312274

[10] Peters, F., "Homogeneous Nucleation of Ethanol and N-Propanol in a Shock Tube," *Journal of Chemical Physics*, Vol. 77, No. 9, Nov. 1982, pp. 4788–4790. doi:10.1063/1.444389

[11] Zahoransky, R., and Peters, F., "Binary Nucleation at Low Temperatures," *Journal of Chemical Physics*, Vol. 83, No. 12, Dec. 1985, pp. 6425–6431. doi:10.1063/1.449542

[12] McDonald, J. E., "Homogeneous Nucleation of Vapor Condensation 1. Thermodynamic Aspects," *American Journal of Physics*, Vol. 30, No. 12, Dec. 1962, pp. 870–877. doi:10.1119/1.1941841

[13] McDonald, J. E., "Homogeneous Nucleation of Vapor Condensation I. Kinetic Aspects," *American Journal of Physics*, Vol. 31, No. 1, Jan. 1963, pp. 31–41. doi:10.1119/1.1969234

[14] Abraham, F., *Homogeneous Nucleation Theory*, Academic Press, New York, 1974, p. 105.

[15] Ivanov, M., Markelov, G., and Gimelshein, S., "Statistical Simulation of Reactive Rarefield Flows: Numerical Approach and Application," AIAA Paper 98-2669, June 1998.

[16] Ashgriz, N., and Poo, J., "Coalescence and Separation in Binary Collisions of Liquid Drops," *Journal of Fluid Mechanics*, Vol. 221, 1990, pp. 183–204. doi:10.1017/S0022112090003536

[17] Benson, C., "An Advanced Model for the Determination of Aerosol Droplet Lifetime in an Inductively Coupled Plasma," Ph.D. Thesis, George Washington University, Washington, D.C., 2002.

[18] Wu, B., Wegener, P., and Stein, G., "Condensation of Sulfur Hexaflouride in Steady Supersonic Nozzle Flow," *Journal of Chemical Physics*, Vol. 68, No. 1, Jan. 1978, pp. 308–318. doi:10.1063/1.435454

[19] Zhong, J., Zeifman, M., and Levin, D., "Sensitivity of Water Condensation in a Supersonic Plume to the Nucleation Rate," *Journal of Thermophysics and Heat Transfer*, Vol. 20, No. 3, July–Sept. 2006, pp. 517–523. doi:10.2514/1.18477

[20] Wolk, J., Strey, R., Heath, C., Wyslouzil, B., "Empirical Function for Homogeneous Water Nucleation Rate," *Journal of Chemical Physics*, Vol. 117, No. 10, 2002, pp. 4954–4960. doi:10.1063/1.1498465

[21] Haberland, H., *Clusters of Atoms and Molecules I: Theory, Experiment, and Clusters of Atoms*, Theoretical Concepts, Springer–Verlag, Berlin/New York/Heidelberg, 1995, p. 422, Chap. 2.